



A square pulse thermorefectance technique for the measurement of thermal properties

February 2022

Changing the World's Energy Future

Yuzhou Wang, Vinay Chauhan, Cody Andrew Dennett, Zilong Hua, Robert S Schley, Daniel J Murray, Marat Khafizov, Geoffrey L Beausoleil, David H Hurley



DISCLAIMER

This information was prepared as an account of work sponsored by an agency of the U.S. Government. Neither the U.S. Government nor any agency thereof, nor any of their employees, makes any warranty, expressed or implied, or assumes any legal liability or responsibility for the accuracy, completeness, or usefulness, of any information, apparatus, product, or process disclosed, or represents that its use would not infringe privately owned rights. References herein to any specific commercial product, process, or service by trade name, trade mark, manufacturer, or otherwise, does not necessarily constitute or imply its endorsement, recommendation, or favoring by the U.S. Government or any agency thereof. The views and opinions of authors expressed herein do not necessarily state or reflect those of the U.S. Government or any agency thereof.

A square pulse thermoreflectance technique for the measurement of thermal properties

Yuzhou Wang, Vinay Chauhan, Cody Andrew Dennett, Zilong Hua, Robert S Schley, Daniel J Murray, Marat Khafizov, Geoffrey L Beausoleil, David H Hurley

February 2022

**Idaho National Laboratory
Idaho Falls, Idaho 83415**

<http://www.inl.gov>

**Prepared for the
U.S. Department of Energy
Under DOE Idaho Operations Office
Contract DE-AC07-05ID14517**

A square pulse thermorefectance technique for the measurement of thermal properties

Yuzhou Wang^{a*}, Vinay Chauhan^b, Zilong Hua^{a*}, Robert Schley^a, Cody A. Dennett^a, Daniel Murray^a, Marat Khafizov^b, Geoffrey Beausoleil II^a, David H. Hurley^{a*}

^a Idaho National Laboratory, Idaho Falls, ID 83415, USA

^b Department of Mechanical and Aerospace Engineering, The Ohio State University, Columbus, OH 43210, USA

Corresponding authors: yuzhou.wang@inl.gov (Y.W), zilong.hua@inl.gov (Z.H.), david.hurley@inl.gov (D.H.)

Abstract

We report on a laser-based square pulse thermorefectance (SPTR) technique for the measurement of thermal properties for a wide range of materials. SPTR adopts the pump-probe thermorefectance principle to monitor the evolution of local temperature after square pulse excitation. The technique features a compact setup, high spatial resolution, and fast data collection. By comparing the acquired SPTR signals with a continuum heat transfer model, material thermal properties can be obtained. Taking advantage of various spot sizes and modulation frequencies, SPTR can measure both the thermal diffusivity and thermal conductivity of poorly to moderately conductive materials and the thermal conductivity of conductive materials with satisfactory accuracy, with potential to be applied to more conductive materials. The technique was validated on three materials: fused silica, single crystal CaF₂ and single crystal nickel (with conductivities ranging from 1-100 W·m⁻¹·K⁻¹) with typical measurement errors of 5-20%. The leading sources of error have been identified by Monte Carlo simulations, and the primary limitations of SPTR are discussed. The compact, fiberized platform we describe here will allow instruments based on this methodology to be deployed in complex, multi-analytical environments for the type of high-throughput correlative analyses that are key to materials design and discovery.

1 Introduction

Understanding the thermal properties of materials is of great importance for emerging energy technologies ranging from thermoelectrics to advanced batteries, fuel cells, and nuclear materials [1-5]. In these applications, temperature control is key functionality for prolonging the service life of essential components. The thermal properties of these energy materials can change significantly depending on composition, structure/microstructure, and aging/usage time [6-10]. It is imperative to understand how heat is transported under various conditions to develop new

1 materials that can meet the increasing demands imposed by these technologies, ranging from
2 advanced thermoelectric to microelectronic materials. Currently, several research programs are
3 underway to accelerate new material discovery through the synergistic integration of experiment
4 and theory [11, 12]. These endeavors call for large matrices of thermal testing, which requires
5 new techniques that can characterize a material's thermal properties in a nondestructive, high-
6 resolution, and high-throughput fashion, allowing relationships between composition,
7 microstructure, and properties to be established in a short time.

8 Traditional steady-state methods and laser flash analysis are the two most commonly used
9 techniques to evaluate thermal properties [13]. Although these conventional techniques have
10 been proven successful on many materials, they require predefined sample geometry, access to
11 the backside of samples, and exhibit limited spatial resolution and are relatively slow due to
12 serial-type data acquisition. Laser-based pump-probe thermoreflectance techniques have been
13 demonstrated as powerful tools for the evaluation of thermal properties for a wide range of
14 materials [14-18]. Thermoreflectance techniques rely on the effect that the optical reflectance is
15 directly proportional to the surface temperature under small temperature changes. In these
16 techniques, a material is heated by an intensity modulated laser (i.e., pump laser), and the
17 temperature-induced reflectivity change at the sample surface is recorded using a second laser
18 (i.e., probe laser). The excitation and detection are conducted on the same side of the material,
19 and there are few restrictions on sample size or shape. By fitting the experimental data of the
20 amplitude and phase profiles of the probe beam to a continuum heat transfer model, thermal
21 transport properties, i.e., thermal conductivity, thermal diffusivity, and interfacial thermal
22 resistance, can be extracted.

23 Combining thermoreflectance techniques with other characterization methods offers a
24 promising solution for the high-throughput screening of new materials. In addition to chemical
25 and microstructural properties from popular methods, such as Raman spectroscopy and electron
26 microscopy, thermoreflectance techniques provide complementary information on
27 thermophysical properties especially important for energy applications. The configuration of
28 collinear source and receiver and small laser spot sizes allow for micrometer-resolution spatial
29 mapping of thermal properties without the need to access the back side of samples [6, 19, 20].
30 Rapid screening combined with chemical and microstructural analysis will provide materials
31 scientists with a powerful tool for developing new materials. Moreover, the interrogation
32 volumes of these microstructure and thermophysical techniques are comparable, enabling a
33 direct correlation between measurement results. The integrated technique described here would
34 accelerate new material discovery by providing straightforward connections between material
35 microstructure, chemical, and thermophysical properties through short, nondestructive analysis.

36 Various techniques based on the thermoreflectance principle have been developed to study
37 thermal properties of bulk materials and thin films. Using ultrafast lasers, the time domain
38 thermoreflectance (TDTR) technique is able to track thermal transport across nanostructures and
39 in multiple directions [14, 21-25]. In frequency domain thermoreflectance (FDTR), both

1 continuous wave (CW) and ultrafast pulsed lasers can be utilized to measure the phase lag of a
2 thermal wave relative to the modulation wave to extract thermal properties [26-28]. In spatial
3 domain thermorefectance (SDTR), the relative position of pump and probe beams are swept to
4 study heat dissipation in isotropic and anisotropic materials [29-32]. A steady state
5 thermorefectance (SSTR) method has also been developed to measure thermal properties by
6 monitoring the temperature rise under different excitation powers and spot sizes [33].

7 Recently, a square pulse thermorefectance (SPTR) technique was proposed to study local heat
8 transport in uranium-nitride/silicide nuclear fuels [19]. This technique utilizes a train of square-
9 wave pump pulses to periodically heat a sample surface and a second probe beam to record the
10 optical reflectance that is proportional to the temperature change as a function of time. SPTR
11 possesses the advantages of thermorefectance techniques, such as high spatial resolution
12 (orders of μm) and short measurement times (order of minutes). **Although the time resolution of**
13 **SPTR is several orders of magnitude larger than TDTR, limiting its applications in certain studies**
14 **such as monitoring the thermal diffusion in the window of nanoseconds [34], SPTR system is**
15 **more cost effective and compact, allowing for possible integration with other instruments to**
16 **provide a multifaceted tool for material characterization and screening [35-37]. Compared to**
17 **FDTR that collects and analyzes the phase profile of the thermal wave using a lock-in amplifier,**
18 **SPTR collects the amplitude profile using an oscilloscope, of which the temperature response due**
19 **to external excitation can be visually observed. These advantages make SPTR an ideal entry point**
20 **for researchers and engineering students to measure and understand thermal transport**
21 **phenomena. With the capability demonstrated and validated in [19], some knowledge gap**
22 **remains when applying SPTR to measure thermal properties, regarding the impacts of sample**
23 **thermal properties, interfacial resistance, and experimental parameters, such as laser spot size,**
24 **transducer film thickness, and modulation frequency, on the measurement results.**

25 In this work, the SPTR technique is further developed and we discuss in detail how to most
26 effectively utilize SPTR to measure material thermal properties. The paper is organized in the
27 following manner: First, the details of experimental implementation and the theory of
28 measurement are described. Next, we investigate the appropriate experimental settings to
29 extract thermal properties based on sensitivity analysis. **Particularly the similar sensitivities to**
30 **the sample's thermal properties and interfacial thermal resistance on conductive materials bring**
31 **challenges to determining each property separately.** Measurement results on fused silica (f-SiO_2),
32 calcium fluoride (CaF_2), and nickel (Ni) are presented and compared with literature values to
33 demonstrate the method's accuracy and reliability. Finally, sources of errors and limitations of
34 the technique are discussed.

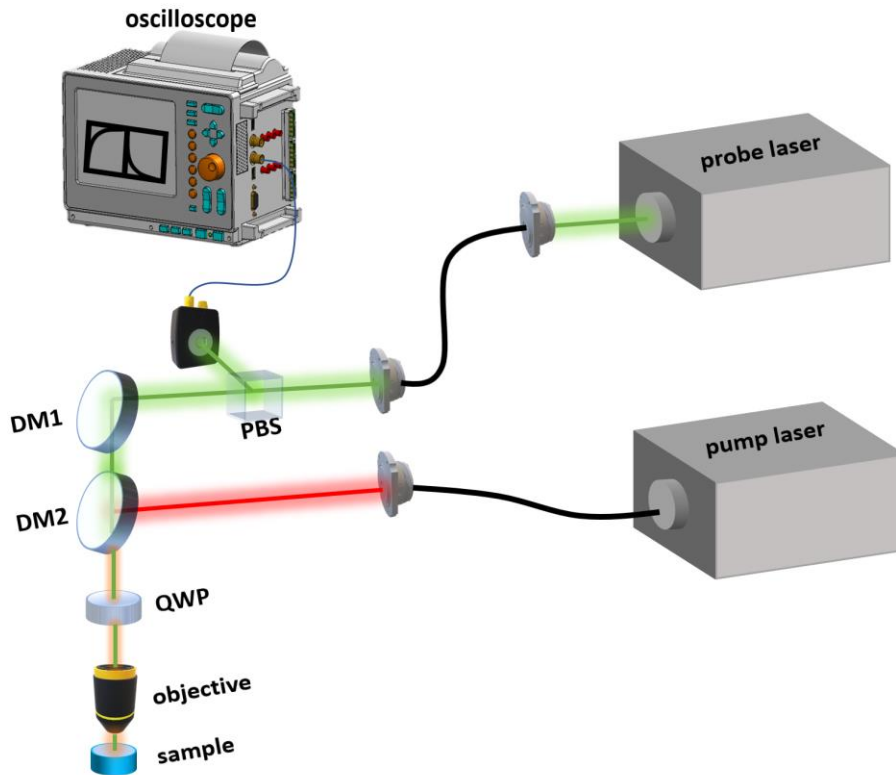
35 2 Experimental setup and theory

36 2.1 Experimental setup

37 The experimental setup of SPTR has been introduced before and is briefly described here (Fig.1)
38 [19, 29]. The pump and probe beams are derived from optical fibers coupled to two CW diode

1 lasers (Coherent Obis) with wavelengths at 660 nm and 532 nm, respectively. In a typical
2 thermorefectance experiment, a thin film of metal (e.g., Au, Al) is deposited on the sample
3 surface to provide extra boundary conditions and act as a transducer to ensure a large
4 thermorefectance coefficient and high optical absorption. Gold was chosen in this work for its
5 large thermorefectance coefficient at 532 nm [38].

6 Both laser beams are coupled to optical fibers and subsequently launched, directed to, and
7 focused on the sample surface by dichroic mirrors and a microscope objective lens. The power of
8 laser beams reaching the sample surface is typically on the order of 1 mW and is adjusted to
9 avoid a large DC temperature rise. The sample is placed on a high precision vertical stage. The
10 polarization-controlled probe beam reflected from the sample surface is directed to a
11 photodiode (Thorlabs PDA36A2 with the amplification setting of 20 dB, corresponding bandwidth
12 1 MHz) through a polarizing beam splitter and the resulting signal is captured by a high-speed
13 digital oscilloscope (Agilent DSO6014A, bandwidth 100 MHz).



14

15 **Fig.1** Design diagram of the experimental setup for SPTR measurement. (DM: dichroic mirror,
16 QWP: quarter waveplate, PBS: polarizing beam splitter)

17 The pump beam amplitude is digitally modulated to have a 50% duty cycle square wave. Two
18 objective lenses with magnifications of 50× and 20× are used in this work. By varying the laser
19 spot size in the measurements, it is possible to measure additional thermal properties besides
20 thermal diffusivity, as will be discussed later. The $1/e^2$ spot radii were measured to be $1.37 \mu\text{m}$

1 and 3.17 μm for both pump and probe beams under the 50 \times and 20 \times objectives, respectively.
 2 The measured signal is averaged over 8000 cycles by the oscilloscope to improve the recorded
 3 signal to noise ratio and to keep the time of measurement for one point to less than one minute.

4 2.2 Theory

5 After the surface temperature signal is recorded by the oscilloscope, the amplitude profile is
 6 compared to a continuum heat transfer model to generate the best fitting thermal properties
 7 using least squares regression. The model describes the surface temperature of a multilayer
 8 structure under a square-wave thermal excitation. First, we decompose square wave $x(t)$ to the
 9 sum of an infinite number of odd harmonic waves [19]

$$x(t) = \sum_{n=-\infty}^{\infty} \frac{\exp(i\omega t(2n-1))}{2n-1}, \quad (1)$$

10 where t is time and ω is the fundamental harmonic frequency. For each harmonic excitation, the
 11 surface temperature response of a two-layer system in the frequency domain has been derived
 12 previously and is given by [22, 39]

$$H(\omega) = \frac{Q}{2\pi} \int_0^{\infty} dp W(\omega, p) \exp\left(\frac{-p^2(r_0^2 + r_1^2)}{8}\right) p, \quad (2)$$

13 where

$$W(\omega, p) = \frac{\frac{\gamma_s m + \gamma_s R_{th} + 1}{\gamma_f}}{\gamma_s + \gamma_f \gamma_s R_{th} m + \gamma_f m}, \quad (3)$$

14 The definition of the parameters in the above equations are listed in Table 1. The subscript
 15 represents either substrate (s) or transducer (f).

16 Table 1. Definition of parameters in the model.

| parameter | definition |
|-----------------|---|
| r_0 and r_1 | 1/e ² radius of pump and probe beams |
| p | spatial Fourier transform coordinate |
| Q | absorbed laser power |
| k | thermal conductivity |
| C | volumetric heat capacity |
| D | thermal diffusivity ($D = \frac{k}{C}$) |
| q | thermal wave vector $q = \sqrt{p^2 + \frac{i\omega}{D}}$ |
| γ | $\gamma = qk$ |
| d_f | film thickness |
| R_{th} | interfacial thermal resistance between the substrate and transducer film |
| m | $m = \tanh(q_f d_f)$ |

17

1 The resulting temperature response in the time domain under a square wave excitation is
 2 obtained by taking the inverse Fourier transform of $H(\omega)$ and summing the harmonics [19]

$$T(t) = \sum_{n=-N}^N H(\omega(2n-1)) \frac{\exp(i\omega t(2n-1))}{2n-1} \text{sinc}\left(\frac{n}{2N}\right). \quad (4)$$

3 We find that it is sufficient to take integration limit as $N = 100$ as the amplitudes of higher
 4 harmonics are negligible. The last term in Eq.(4) is the Lanczos sigma factor to remove the
 5 undesired Gibbs phenomenon (i.e., ringing effect) often observed in signal processing.

6 When the modulation frequency is close to the bandwidth of the photodetector, high-order
 7 harmonics will be filtered out, resulting in the distortion of both the pump and probe signal. To
 8 account for this, we need to modify the model to analyze the data of imperfect high frequency
 9 square pulses by introducing corrections to Eq.(4):

$$T'(t) = \sum_{n=-N}^N H(\omega(2n-1)) \frac{\exp(i\omega t(2n-1))}{2n-1} \text{sinc}\left(\frac{n}{2N}\right) P \exp(i\phi) \quad (5)$$

10 where P and ϕ are the amplitude and phase of the correction function, respectively. These
 11 parameters depend on the specifics of experimental instruments and frequency. The derivation
 12 of these parameters and the impact will be given in the last section and the appendix.

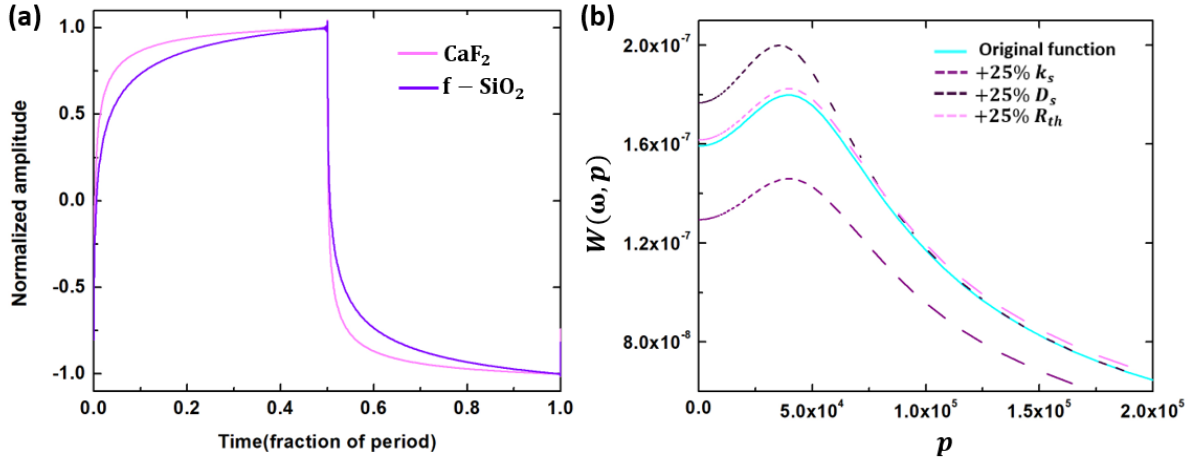
13 The samples in this work include f-SiO₂, CaF₂, and Ni. F-SiO₂ has a relatively small thermal
 14 conductivity (1.38 W·m⁻¹·K⁻¹, 0.83 mm²·s⁻¹) and represents the lower bound in this study; CaF₂
 15 has moderate thermal properties (9.71 W·m⁻¹·K⁻¹, 3.58 mm²·s⁻¹); and Ni represents energy
 16 materials with relatively high thermal conductivity (90.7 W·m⁻¹·K⁻¹, 23.0 mm²·s⁻¹).

17 The thermal conductivity of gold films has been found to be very sensitive to the film thickness
 18 [40, 41]. To accurately measure this value, BK7 standards were deposited with gold in tandem
 19 with the samples of interest. The conductivities of these Au films on BK7, which were co-
 20 deposited with the samples, were measured separately using SDTR.

21 An example SPTR signal is simulated using the model described in Eq.(4) and presented in Fig.2(a).
 22 The model parameters are provided in the caption [42]. The square pulse response is normalized
 23 by the maximum amplitude and the length of one cycle. It is noted here that, depending on the
 24 length of period or modulation frequency, the surface temperature may or may not reach a
 25 steady state at the middle of the cycle. **Whether the signal reaches steady state does not impact**
 26 **the results, as the largest sensitivity to thermal properties is provided by the rising/falling**
 27 **sections that promptly follow the incidence/removal of pump pulse as demonstrated later.** As
 28 soon as the pump laser is turned off, the temperature drops quickly and then slowly returns to
 29 minimum level at the end of the period. The rising and falling curves should be identical based
 30 on the model. Over the square pulse cycle, the same amount of energy can be imparted to or
 31 removed from the system, both of which have the same mathematical expressions except for the
 32 sign of Q in Eq.(2).

33 The shape of the response signal is extremely sensitive to a material's thermal properties. For
 34 CaF₂, the observed temperature change is much faster than that of f-SiO₂. This indicates that heat

1 is transported faster in CaF₂ compared to f-SiO₂. Following this logic, one possible application for
 2 the SPTR technique is to provide an instant comparison of materials' thermal properties by
 3 comparing the rising of amplitude in the time domain (assuming measurements are performed
 4 with identical experimental conditions).



5
 6 **Fig.2** (a) Theoretical SPTR response on CaF₂ and f-SiO₂ coated with a 36 nm gold transducer film
 7 at the modulation frequency of 10 kHz. For these calculations, the interfacial thermal resistance
 8 is set to $1 \times 10^{-8} \text{ m}^2 \cdot \text{K} \cdot \text{W}^{-1}$, the film conductivity to $128 \text{ W} \cdot \text{m}^{-1} \cdot \text{K}^{-1}$, and spot size is $1.37 \mu\text{m}$. (b) The
 9 function $W(\omega, p)$ simulated on 41 nm gold coated on Ni using a 10 kHz modulation frequency
 10 and $50\times$ objective. p is the Fourier transform factor of radial coordinate. The dash lines
 11 correspond to 25% changes to R_{th} , k_s , and D_s .

12 3 Sensitivity analysis

13 As the model indicates, the temperature response is determined by several parameters (i.e.
 14 thermal properties of the transducer film and substrate, modulation frequency, and laser spot).
 15 These properties impact the result in a complex manner; thus it is important to investigate each
 16 parameter separately to determine optimal experimental settings and the range of thermal
 17 properties that can be evaluated accurately.

18 For materials with low or moderate thermal conductivities, numerical calculation indicates that
 19 Eq.(3) can be simplified to the following form

$$W_L(\omega, p) \approx \frac{1}{\gamma_s} \times \frac{1}{1+m(\gamma_f R_{th} + \frac{\gamma_f}{\gamma_s})} \quad (6)$$

20 For a thermally thin transducer film with a thickness much smaller than the thermal diffusion
 21 length, $\sqrt{2D_s/\omega}$, the parameter m approaches zero such that terms containing m can be omitted.
 22 In this limit, $W_L(\omega, p)$ is thus solely determined by substrate thermal properties.

1 For materials with high thermal conductivity (close to or above $100 \text{ W}\cdot\text{m}^{-1}\cdot\text{K}^{-1}$), the simplifications
 2 taken to derive Eq.(6) no longer hold and Eq.(3) can be alternatively transformed to the following
 3 form

$$W_H(\omega, p) \approx \frac{1+\gamma_s R_{th}}{\gamma_s + \gamma_s \gamma_f R_{th} m}. \quad (7)$$

4 For thermally thin films, the terms containing m can also be safely ignored to obtain

$$W_H(\omega, p) \approx R_{th} + \frac{1}{\gamma_s}. \quad (8)$$

5 In this limit the film doesn't impact the resulting time-dependent profile. However, the interfacial
 6 resistance cannot be ignored and must be considered when extracting material thermal
 7 properties. When the modulation frequency increases, the thermal diffusion length will decrease
 8 and approach the transducer film thickness such that $W(\omega, p)$ will be more coupled to both the
 9 film and interfacial properties.

10 To understand the impact of spot size on the SPTR signal, we plot the simulated function $W(\omega, p)$
 11 for 41 nm gold coated Ni under 10 kHz modulation frequency in Fig.2(b). In addition, the same
 12 function with 25% variations to R_{th} , k_s , or D_s are also presented in the same figure. From
 13 Fig.2(b), the impact of D_s is confined to the region where the spatial Fourier parameter p is less
 14 than 1×10^5 , whereas R_{th} and k_s impact the response $W(\omega, p)$ over a very broad range of p .
 15 According to Eq.(2), the frequency response $H(\omega, p)$ is obtained by convolving $W(\omega, p)$ with
 16 Fourier transformed Gaussian spot profile. A large laser spot will reduce the weighting of large p
 17 in the integration of Eq.(2), diminishing the impact of film and interfacial resistance while
 18 improving the sensitivity to D_s . As a result, it is possible to take advantage of different spot sizes
 19 and determine multiple thermal properties of a given, fixed layered structure [16, 33, 39].

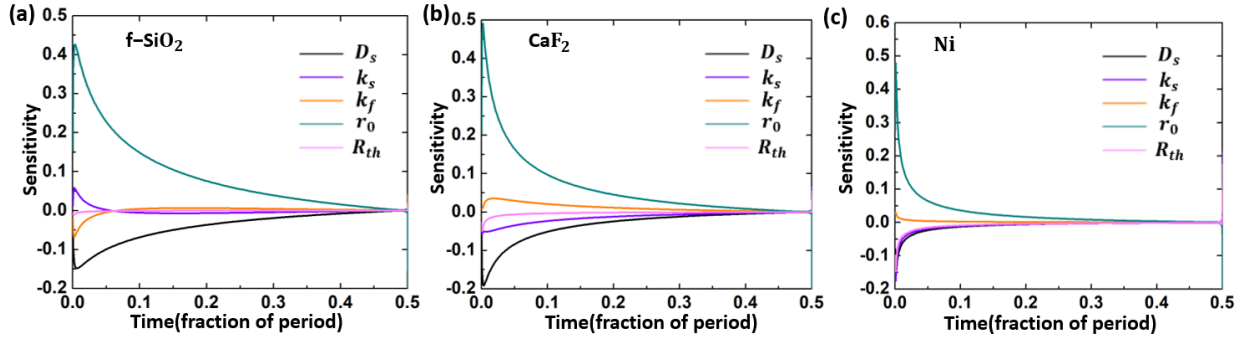
20 To explicitly describe the impact of each parameter ξ , we define a sensitivity function as [29]

$$S_\xi(t) = \frac{\partial T(t)}{\partial \xi} = \frac{T(\Delta\xi + \xi, t) - T(\xi, t)}{\Delta\xi / \xi}. \quad (9)$$

21 The function $S_\xi(t)$ for 36 nm gold coated f-SiO₂, 82 nm gold coated CaF₂, and 41 nm gold coated
 22 Ni are presented in Fig.3, where ξ includes thermal diffusivity, D , and conductivity, k , for both
 23 film and substrate, as well as laser spot radius and interfacial thermal resistance R_{th} between the
 24 transducer film and substrate. These film thicknesses are chosen to ensure large sensitivity to
 25 substrate thermal properties based on Fig.4 and related discussions in the following analysis. The
 26 interfacial thermal resistance is set to $1 \times 10^{-8} \text{ m}^2\cdot\text{K}\cdot\text{W}^{-1}$, typical in the range of previous
 27 measurements [43]. The thermal conductivities of transducer films on f-SiO₂, CaF₂, and Ni are 128
 28 $\text{W}\cdot\text{m}^{-1}\cdot\text{K}^{-1}$, $133.6 \text{ W}\cdot\text{m}^{-1}\cdot\text{K}^{-1}$, and $130.9 \text{ W}\cdot\text{m}^{-1}\cdot\text{K}^{-1}$, respectively, based on SDTR measurements.
 29 Only half a cycle is presented since the second half carries the same information based on Fig.2(a).

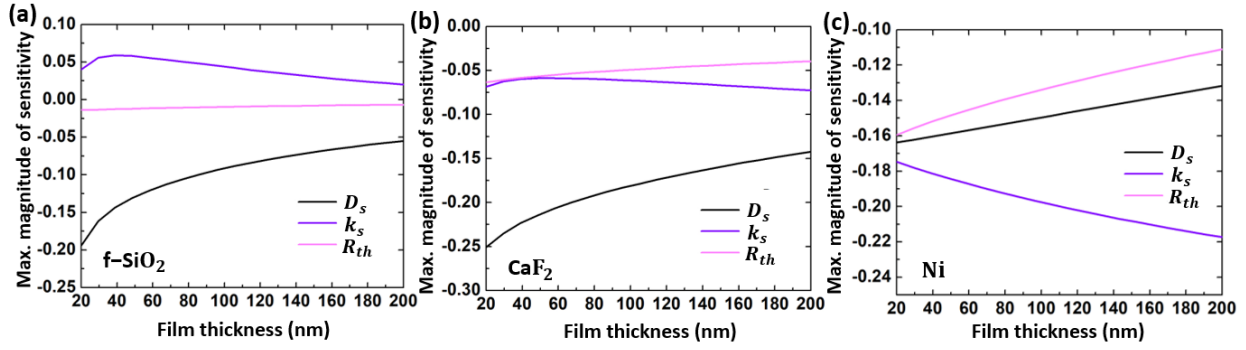
30 As is clearly illustrated in Fig.3, most of the changes happen during the fast-rising section of the
 31 square wave period (before one tenth of a period). In addition, the spot size has a very large
 32 impact on the overall result and should be measured accurately [28, 33]. In fact, for most
 33 experimental configurations, spot size has a dominant impact on the temperature response and

1 is the most important experimental parameter as well as the largest source of error. The rise time
 2 τ of the temperature response can be roughly approximated by $\tau = \frac{C_f r^2}{3k_s}$ [19]. Only the spot
 3 radius has a parabolic relationship to τ whereas the rest of material properties have a first-order
 4 relationship. An inaccurate spot size could induce large error to the fitting results; this
 5 dependence will be discussed in detail in the final section.



6 **Fig.3** Sensitivity analysis on f-SiO₂, CaF₂, and Ni at a modulation frequency of 10 kHz, using the
 7 50× objective. (a) f-SiO₂ coated with 36 nm gold; (b) CaF₂ coated with 82 nm gold; (c) Ni coated
 8 with 41 nm gold.
 9

10 For f-SiO₂ and CaF₂, the transducer films are thermally thin such that they only have a limited
 11 impact on the measured response. Besides spot size, substrate thermal diffusivity has the largest
 12 impact. The sensitivity to the substrate thermal conductivity is low but non-negligible, as the
 13 convolved spot size is comparable with thermal diffusion length, resulting in some degree of
 14 radial thermal transport [39]. Thus, it is difficult to distinguish thermal conductivity and diffusivity
 15 from a single SPTR measurement. For Ni, the impact of the interface increases significantly in
 16 accordance with Eq.(8). **As Fig.3(c) shows, sensitivities of interfacial thermal resistance and**
 17 **substrate conductivity have comparable amplitudes over most of the period. It can be explained**
 18 **through a “serial thermal resistance” model [44], by considering both the film and substrate as**
 19 **two thermal resistances serially connected by the interfacial resistance. Compared to other**
 20 **substrates used in this study, larger thermal conductivity of Ni makes its thermal resistance**
 21 **significantly smaller and become comparable to the interfacial thermal resistance. Therefore, the**
 22 **extraction of interfacial thermal resistance is only possible on Ni, if its impact on the signal can**
 23 **be separated from the one from the Ni substrate thermal conductivity.**



1

2 **Fig.4** Maximum magnitude of sensitivity function S_ξ for thermal conductivity, diffusivity, spot
 3 size, and interfacial resistance vs gold film thickness (at 10 kHz frequency and using the 50×
 4 objective). (a)f-SiO₂, (b) CaF₂, (c) Ni.

5 To investigate the impact of transducer film thickness on the sensitivities of thermal properties,
 6 we calculate the maximum magnitude of the sensitivity function S_ξ for our test samples and for
 7 film thicknesses in the range of 20-200 nm (Fig.4). This range of film thicknesses is typical of
 8 thermoreflectance measurements. The thermal conductivity of gold film is based on the
 9 interpolation of results independently measured on gold films with various thicknesses. The
 10 modulation frequency is set to 10 kHz and the objective magnification is 50×. The maximum
 11 magnitude of sensitivity S_ξ is defined as the value with the largest absolute magnitude of a
 12 sensitivity function in a single period. For example, the maximum magnitude of sensitivity S_{D_s} in
 13 Fig.3(a) is -0.15. Other controlled parameters, such as the thickness and thermal conductivity of
 14 transducer film, can be determined separately and are not discussed here. In the subsequent
 15 discussion, unless explicitly stated, the absolute values of sensitivity function are used. However,
 16 the sign of S_ξ is also important as it indicates the correlation between different properties.

17 For f-SiO₂ and CaF₂, the impact of film thickness is greatest on S_{D_s} according to Fig.4(a-b). The
 18 sensitivity of thermal diffusivity decreases significantly for a thicker gold film. The sensitivity of
 19 interfacial thermal resistance is minimally impacted for f-SiO₂ and slightly decreases for CaF₂. For
 20 f-SiO₂, the sensitivity S_{k_s} increases until 50 nm and then starts to decrease. In contrast, the
 21 sensitivity S_{k_s} of CaF₂ decreases at first and then slowly increases with the film thickness. The S_{k_s}
 22 of f-SiO₂ and CaF₂ have opposite signs. To measure the thermal properties of f-SiO₂, film thickness
 23 around 40 nm corresponding to large sensitivities of k_s and D_s is appropriate. As for CaF₂, in
 24 addition to the sensitivities of thermal properties, the impact of interface needs to be minimized.
 25 Therefore, we chose film thickness around 90 nm in this study.

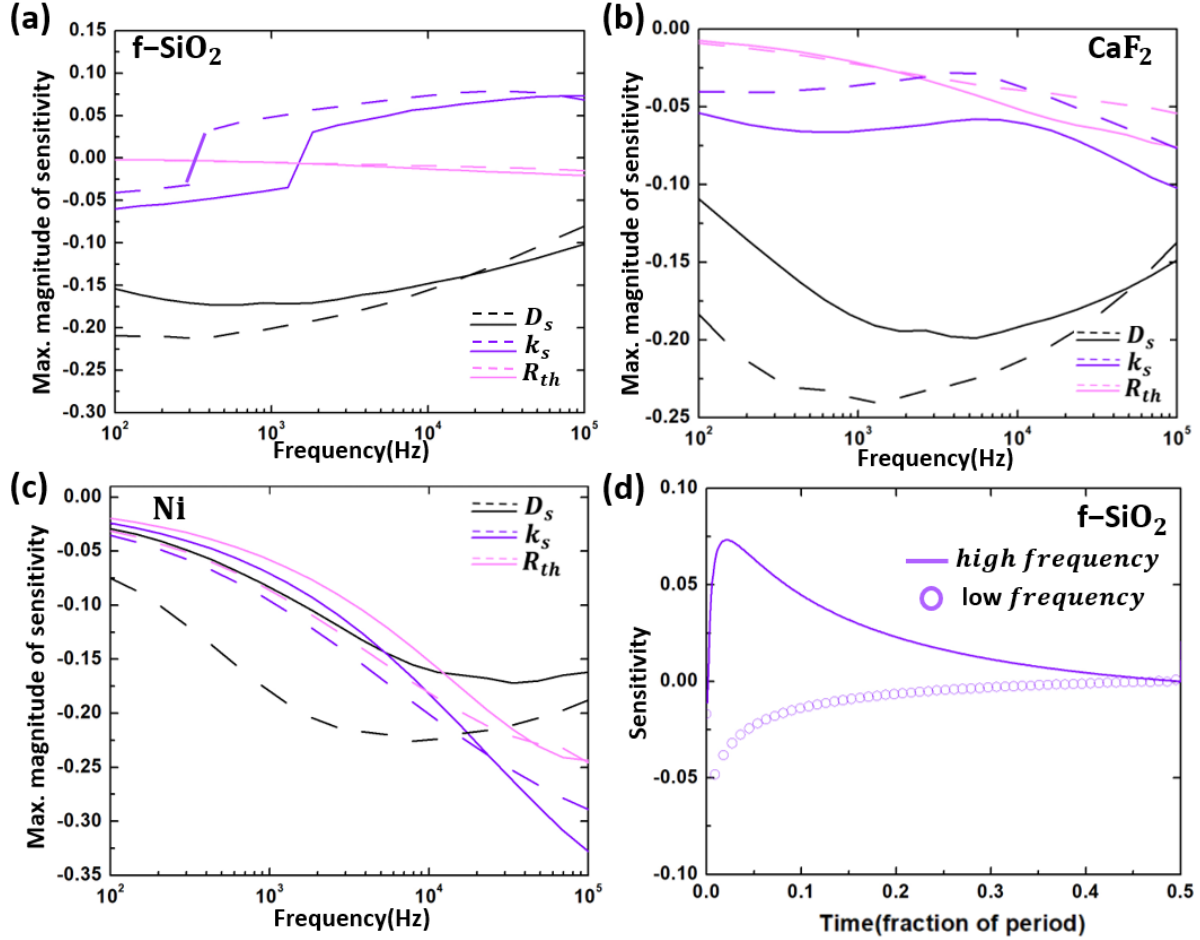
26 From the results in Fig.4(c), the impact of film thickness on Ni is generally limited. The sensitivity
 27 S_{k_s} increases slightly and sensitivity S_{D_s} decreases slightly with an increasing film thickness. For
 28 these reasons, on highly conductive materials, film thicknesses smaller than 100 nm are
 29 appropriate to ensure a large sensitivity to substrate thermal properties. To minimize the impact

1 of substrate on the signal, the thickness of transducer should be at least on the order of optical
2 penetration depth for both pump and probe light in Au.

3 To further investigate the impact of spot size and modulation frequency on the sensitivities of
4 thermal properties, we calculate the maximum magnitude of sensitivity function S_{ξ} for the
5 aforementioned three samples in the frequency range of 10^2 - 10^5 Hz and under two microscope
6 objectives and present the results in Fig.5. The lower frequency limit is set here by the detector
7 noise level while the higher boundary is limited by the detector bandwidth [45].

8 According to Fig.5, for larger spot sizes, the sensitivity to substrate thermal diffusivity is generally
9 improved whilst the sensitivities to all other parameters are suppressed, in agreement with the
10 conclusions of Fig.2(b). For materials with poor thermal conductivity, such as f-SiO₂, the impact
11 of the interface is limited over a broad range of frequencies and can be safely ignored in the data
12 analysis. The impact for thermal diffusivity is the strongest near 1 kHz for the 50× objective or
13 400 Hz for 20× objective. These frequencies also correspond to the smallest sensitivity to thermal
14 conductivity. Far away from these frequencies the sensitivity to conductivity is improved whereas
15 that of thermal diffusivity drops, thus bringing their sensitivities to a comparable level. The abrupt
16 crossover of the maximum magnitude for S_{k_s} from negative to positive value around 1 kHz in
17 Fig.5(a) is due to the change of S_{k_s} shape illustrated in Fig.5(d). At low frequencies, the values of
18 S_{k_s} are negative (symbols in Fig.5(d)); in contrast, the shape of S_{k_s} is flipped around the x axis at
19 a high frequency and the maximum magnitude becomes positive (solid line in Fig.5(d)).

20 For moderately conductive materials such as CaF₂, interfacial thermal resistance only affects the
21 SPTR temperature profile on the higher end of the considered frequency range. Therefore, to
22 reduce its influence when measuring material thermal properties, it is sufficient to avoid high
23 frequencies. The frequencies corresponding to the largest and smallest sensitivities to thermal
24 diffusivity and conductivity increase compared to those of f-SiO₂. Finally, for very conductive
25 materials such as Ni, the sensitivity of interface has a comparable amplitude to those of thermal
26 properties over a broad range of frequency and should be accounted for when extracting
27 material thermal properties.



1

2 **Fig. 5** Maximum magnitude of sensitivity function S_ξ for thermal conductivity, diffusivity, and
 3 interfacial thermal resistance vs modulation frequency (magnifications of objective are 50×
 4 (solid line) and 20× (dash line)). (a) 36 nm gold coated f-SiO₂, (b) 82 nm gold coated CaF₂, (c) 41
 5 nm gold coated Ni, and (d) shapes of sensitivity function S_{k_s} for f-SiO₂ at low (100 Hz) and high
 6 (100 kHz) frequency. The small kinks in some curves are numerical artifacts; the true peak
 7 position of S_ξ may not be captured by the simulation due to its sharpness.

8 We recall that the primary objective of this work is to develop a reliable methodology to measure
 9 substrate thermal properties. The above sensitivity analysis suggests that the measurement
 10 accuracy depends on the ability to properly account for the interfacial thermal resistance. One
 11 single SPTR measurement is not sufficient to determine all of the three unknown thermal
 12 properties (D_s , k_s , and R_{th}) that impact the temperature evolution. Some combinations of two
 13 thermal properties may be determined by analyzing several measurements in different
 14 frequency ranges. The determination of all three thermal properties proves to be challenging for
 15 the current SPTR configuration.

16 Furthermore, the sensitivity analysis in Fig.3-5 indicates that the experimental settings should be
 17 chosen based on the specific material properties to ensure the largest sensitivity to the interested

1 properties and the smallest sensitivity to the undesired ones. A large sensitivity corresponds to
2 small errors when extracting thermal properties from experimental data using a multilayer
3 thermal transport model. This especially applies to the experimental settings on poorly or
4 moderately conductive materials to ensure the sensitivity of interfacial thermal resistance is
5 negligible. If the interfacial thermal resistance has a non-negligible sensitivity in a wide range of
6 settings, for example on Ni, it is appropriate to choose settings that have enough sensitivity to
7 the material thermal properties and interfacial thermal resistance so that both quantities can be
8 determined accurately.

9 The optimal experimental settings based on the material thermal properties are summarized in
10 Table 2. For a completely unknown material, thermal properties can first be roughly estimated
11 based on the method of Fig.2(a) by comparing the temperature rise time with tabulated results.
12 Afterwards, experimental settings may be shifted based on the recommendations below to make
13 high-confidence measurements of the properties of interest.

14 If the material heat capacity is already known, the number of unknown thermal parameters is
15 reduced to two, namely D_s and R_{th} . The thermal diffusivity of f-SiO₂ and CaF₂ can be directly
16 obtained from a single measurement of appropriate spot size and frequency that correspond to
17 a large sensitivity to D_s and very small sensitivity to R_{th} , such as 1 kHz and 20× objective in
18 Fig.5(b). Moreover, the gold film should be thin enough to ensure enough sensitivity to D_s
19 according to Fig.4(a-b).

20 On the other hand, if heat capacity is unknown, we can take advantage of the distinct sensitivities
21 at different settings and combine two measurements to extract both D_s and k_s . The method to
22 analyze these sets of data is analogous to the simultaneous determination of several parameters
23 in FDTR and TDTR [16, 39]. Although many combinations of material properties can explain the
24 experimentally obtained temperature response under each experimental setting, the true
25 material properties should be able to generate temperature responses from modeling that can
26 satisfactorily match the experimental results of all combinations of spot sizes and frequencies.
27 The experimental settings should be carefully selected such that the ratios of sensitivities
28 between D_s and k_s are distinct for both cases while maintaining as low a sensitivity to R_{th} as
29 possible. As illustrated in the experimental validation section, the distinct ratios of sensitivity
30 allow for the D_s vs k_s curves of two data sets to intersect at a clear point. This can be
31 conveniently achieved by adjusting spot size and modulation frequency based on the sensitivity
32 analysis in Fig.5. The thickness of the applied gold transducer film is not convenient to change in
33 experiments compared to spot size or frequency, and therefore should be selected in the range
34 where sensitivities of D_s and k_s have comparable and large amplitudes.

35 For highly conductive materials, R_{th} needs to be considered at most frequencies and heat
36 capacity needs to be known a priori to eliminate one unknown quantity. Two measurements are
37 required to resolve both D_s and R_{th} . The experimental settings should be carefully selected so
38 that in one setting, the sensitivity ratio of D_s and R_{th} is distinct from that in the other setting. A

1 large film thickness should be avoided as both the sensitivities of D_s and R_{th} decrease with film
 2 thickness, as shown Fig.4(c).

3 Table 2. Optimal experimental settings to extract thermal properties. Two settings are given for
 4 some cases that have distinct sensitivities for interested parameters.

| material thermal conductivity | when heat capacity is known | when heat capacity is unknown |
|--|--|---|
| $\mathcal{O}(1 \text{ W}\cdot\text{m}^{-1}\cdot\text{K}^{-1})$ | Large spot size (20× obj.) and thin transducer (<30 nm); frequency is chosen based on sensitivity analysis (generally below 1 kHz) | Moderate transducer thickness (30 nm < d_f < 100 nm); a) large spot (20× obj.) and low frequency (<1 kHz), or b) small spot (50× obj.) and high frequency (>1 kHz) |
| $\mathcal{O}(10 \text{ W}\cdot\text{m}^{-1}\cdot\text{K}^{-1})$ | Large spot size (20× obj.) and thin transducer (<30 nm); frequency is chosen based on sensitivity analysis (generally below 1 kHz) | Moderate transducer thickness (30 nm < d_f < 100 nm); a) large spot (20× obj.) and low frequency (<1 kHz) or b) small spot (50× obj.) and moderate frequency (1 kHz < f < 10 kHz) |
| $\mathcal{O}(100 \text{ W}\cdot\text{m}^{-1}\cdot\text{K}^{-1})$ | Small to moderate film thickness (<100 nm); a) large spot (20× obj.) and low frequency (<10 kHz), or b) small spot (50× obj.) and high frequency (>20 kHz) | n/a |

5

6 4 Experimental validation

7 In this section we validate the SPTR technique on several materials listed in Table 3. Validation
 8 measurements are separated into two categories. First, we focus on measurements of materials
 9 where the heat capacity is known. Second, we evaluate thermal properties when heat capacity
 10 is unknown. Ten measurements were taken in each case and the standard deviation between
 11 this set of measurements was taken as the ultimate error.

12 4.1 Measuring materials with known heat capacity

13 There are many established means to obtain the heat capacity of a material of interest, such as
 14 differential scanning calorimetry and calculations from the Kopp–Neumann law and phase field
 15 methods[46]. Oftentimes heat capacity is not impacted much by sample size or small
 16 microstructural variations and can be taken directly from literature values [46, 47]. In such cases,
 17 a confident a priori estimate of the heat capacity reduces the unknown thermal properties and
 18 simplifies the ultimate determination of D_s .

19 Test samples for the validation of the SPTR method were prepared for f-SiO₂, CaF₂, and Ni. The
 20 thicknesses of the gold transducer films deposited on f-SiO₂, CaF₂, and Ni samples are 36 nm, 82
 21 nm, and 41 nm, respectively. These films ensure a large sensitivity to D_s according to Fig.4(a-c).

1 Their thermal conductivities were measured to be $128 \text{ W}\cdot\text{m}^{-1}\cdot\text{K}^{-1}$, $133.6 \text{ W}\cdot\text{m}^{-1}\cdot\text{K}^{-1}$, and 130.9
 2 $\text{W}\cdot\text{m}^{-1}\cdot\text{K}^{-1}$, respectively.

3 For poorly or moderately conductive materials, the thermal diffusivity can be straightforwardly
 4 calculated in the frequency range where the impact of interface thermal resistance is negligible.
 5 To measure the thermal diffusivity of f-SiO₂, we chose a 20× objective and 400 Hz to take
 6 advantage of the corresponding large D_s sensitivity. For CaF₂, we chose a 20× objective and 1 kHz
 7 for the high sensitivity to D_s . A typical value in the range of previously measured thermal
 8 resistance between metals and dielectrics was set for the interfacial thermal resistance, for
 9 example, $R_{th} = 1 \times 10^{-8} \text{ m}^2\cdot\text{K}\cdot\text{W}^{-1}$, which has limited impact as the model indicates [43].

10 The experimental and model fitting results are presented in Fig.6(a-b). We find a very good
 11 agreement between the experiment and the model. The fitting values of substrate diffusivity are
 12 $0.83 \pm 0.31 \text{ mm}^2\cdot\text{s}^{-1}$ and $3.89 \pm 0.51 \text{ mm}^2\cdot\text{s}^{-1}$ for f-SiO₂ and CaF₂, respectively. Taking literature
 13 values of heat capacity, their thermal conductivities are calculated to be $1.38 \pm 0.51 \text{ W}\cdot\text{m}^{-1}\cdot\text{K}^{-1}$
 14 and $10.54 \pm 1.39 \text{ W}\cdot\text{m}^{-1}\cdot\text{K}^{-1}$. These values agree closely with previously reported thermal
 15 properties as shown in Table 3. The larger error associated with SPTR measurement on f-SiO₂ is
 16 attributed to Au film agglomeration[40].

17 To illustrate the large errors originating from inappropriate experimental settings, we also
 18 conducted measurements on f-SiO₂ with parameters deliberately chosen to reduce the sensitivity
 19 to the desired thermal properties. Here, we used a large film thickness (203 nm), 20× objective,
 20 and 100 kHz frequency to measure the thermal conductivity assuming the heat capacity is known.
 21 According to the analysis in Fig.4-5, the sensitivity of thermal diffusivity is very small such that an
 22 inaccurate result is expected. This is confirmed by the measurement result which yields a thermal
 23 conductivity of $2.16 \pm 0.52 \text{ W}\cdot\text{m}^{-1}\cdot\text{K}^{-1}$ on f-SiO₂ with inappropriate settings.

24

25 Table 3. Measured and literature values of thermal conductivity (k) and thermal diffusivity (D).

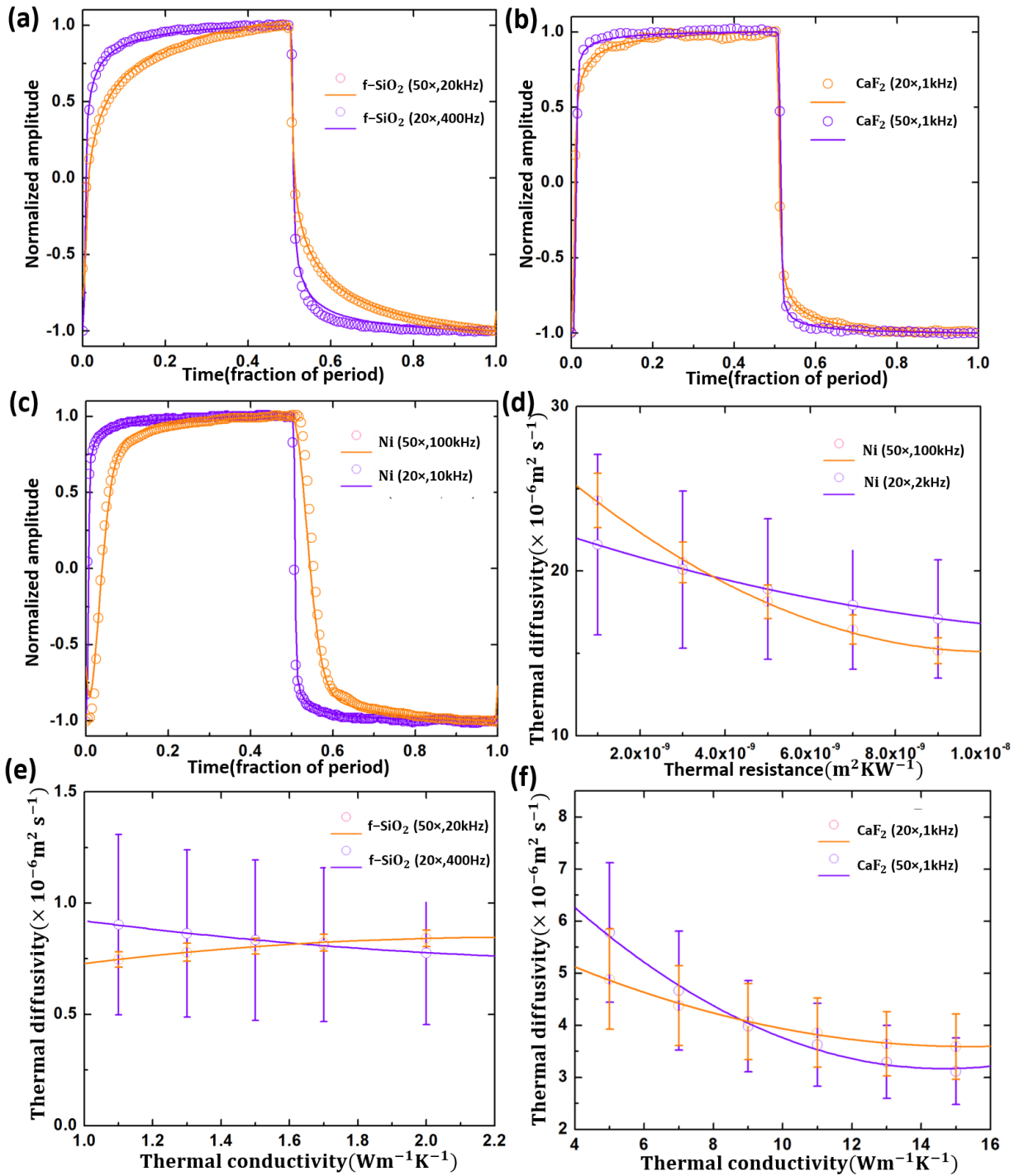
| Samples (transducer thickness) | Literature Values [29, 42, 46] | | Heat Capacity Is Known | | Heat Capacity Is Unknown | |
|--------------------------------------|---|------------------------------------|---|------------------------------------|---|------------------------------------|
| | $k(\text{W}\cdot\text{m}^{-1}\cdot\text{K}^{-1})$ | $D(\text{mm}^2\cdot\text{s}^{-1})$ | $k(\text{W}\cdot\text{m}^{-1}\cdot\text{K}^{-1})$ | $D(\text{mm}^2\cdot\text{s}^{-1})$ | $k(\text{W}\cdot\text{m}^{-1}\cdot\text{K}^{-1})$ | $D(\text{mm}^2\cdot\text{s}^{-1})$ |
| f-SiO ₂ (36 nm) | 1.38 | 0.83 | 1.38 ± 0.51 | 0.83 ± 0.31 | 1.63 ± 0.52 | 0.82 ± 0.26 |
| CaF ₂ (82 nm) | 9.71 | 3.58 | 10.54 ± 1.39 | 3.89 ± 0.51 | 8.81 ± 1.76 | 4.10 ± 0.82 |
| Ni (41 nm) | 90.7 | 23.0 | 77.46 ± 14.41 | 19.66 ± 3.66 | n/a | n/a |

26

27 Next, the thermal diffusivity of Ni is evaluated. Although the film (41 nm) is thermally thin
 28 compared to its thermal diffusion length and the spot size is large when using a 20× objective,
 29 the analysis from Eq.(8), as well as Fig.5(c), indicates that the interface cannot be ignored for

1 materials with large thermal conductivity. We take the heat capacity and density of Ni as known
2 parameters from literature [42]. With these fixed parameters, the model has two fitting
3 parameters, namely interfacial thermal resistance and substrate thermal diffusivity. To take
4 advantage of the distinct sensitivities in Fig.5(c), two sets of experimental data were taken for
5 20× objective, 2 kHz and 50× objective, 100 kHz. Next, a range of values for interfacial thermal
6 resistance were applied to the model to fit the experimental data in Fig.6(c), and the
7 corresponding best-fitting thermal diffusivities were obtained. In Fig.6(d), we plot these two sets
8 of data in the same figure. The points are connected by polynomial lines fitted to the
9 experimental data. The crossing point is at $R_{th} = 3.71 \times 10^{-9} \text{ m}^2 \cdot \text{K} \cdot \text{W}^{-1}$, $D_s = 19.66 \times 10^{-6}$
10 $\text{m}^2 \cdot \text{s}^{-1}$. The error at this point was calculated by taking the root mean square of the errors of both
11 parameters at nearby points. Taking the volumetric heat capacity of Ni as $C = 3.94 \times 10^6 \text{ J} \cdot \text{m}^{-3} \cdot \text{K}^{-1}$,
12 the thermal conductivity of Ni is estimated to be $k_s = D_s \times C_s = 77.46 \text{ W} \cdot \text{m}^{-1} \cdot \text{K}^{-1}$. The
13 interfacial thermal resistance is on the same order as previously reported values between gold
14 and other metals [48, 49]. In Fig.6(d), the curve corresponding to 20× objective, 2 kHz has a
15 smaller slope compared to the curve for 50× objective, 100 kHz, which can be explained by the
16 different sensitivities illustrated in Fig.5(c). The ratio of sensitivity between D_s and R_{th} for 20×
17 objective and 2 kHz is larger than that for 50× objective and 100 kHz. As a result, to compensate
18 for the same amount of change in R_{th} , the change of D_s is larger for the case of 50× objective
19 and 100 kHz.

20



2

3 **Fig. 6** Experimental and model fitting results. Open circles correspond to the experimental
 4 result, and a solid line is the model result. (a) f-SiO₂ coated with 36 nm gold, 20× objective, 400
 5 Hz (purple) and 50× objective, 20 kHz (orange); (b) CaF₂ coated with 82 nm gold, 50× objective,
 6 1 kHz (purple), and 20× objective, 1kHz (orange); (c) Ni coated with 41 nm gold, 20× objective, 2
 7 kHz (purple), and 50× objective, 100 kHz (orange); (d) R_{th} vs D_s curves for two data sets

1 measured on Ni sample; (e) k_s vs D_s curves for two data sets measured on f-SiO₂ sample; (f) k_s vs
2 D_s curves for two data sets measured on CaF₂ sample.

3 4.2 Measuring materials with unknown heat capacity

4 To resolve the thermal conductivity and diffusivity of f-SiO₂ and CaF₂ when the material heat
5 capacity is unknown, multiple measurements are required to ensure a larger sensitivity to
6 thermal conductivity. For f-SiO₂, additional measurements with a 50× objective and 20 kHz
7 frequency were collected; measurements using a 50× objective and 1 kHz frequency were
8 collected as the secondary data set for CaF₂. These settings ensure larger sensitivity to thermal
9 conductivity as demonstrated in Fig.5(a-b) while the impact of interface is negligible. The film
10 thicknesses also ensure there is enough sensitivity to k_s according to Fig.4(a-b).

11 The method to extract both k_s and D_s is similar to that of Ni described above. Rather than fitting
12 D_s as a function of R_{th} , it was fitted as a function of thermal conductivity k_s . Examples of fitted
13 model are presented in Fig.6(a-b). The extracted k_s vs D_s results are plotted in Fig.6(e-f). The
14 crossing point for f-SiO₂ is $k_s = 1.63 \text{ W}\cdot\text{m}^{-1}\cdot\text{K}^{-1}$, and $D_s = 0.82 \text{ mm}^2\cdot\text{s}^{-1}$. For CaF₂, the two curves
15 intersect at $k_s = 8.81 \text{ W}\cdot\text{m}^{-1}\cdot\text{K}^{-1}$, and $D_s = 4.10 \text{ mm}^2\cdot\text{s}^{-1}$. These results generally have larger
16 errors compared with the values in the previous section due to more unknown properties but
17 are still within the range of errors from measurements taken when the heat capacity is known a
18 priori. From the simultaneous determination of D_s and k_s , we are also able to estimate the
19 volumetric heat capacity C_s .

20 We note that only the slope of k_s vs D_s curve for f-SiO₂ under a 50× objective and 20 kHz
21 frequency is positive while the rest curves have negative slopes. This can be explained by the
22 sensitivity analysis in Fig.5(a). Under these experimental conditions, the sensitivities of k_s and D_s
23 have opposite signs in Fig.5(a), resulting in a positive correlation relation between k_s and D_s
24 when fitting to the data. On the other hand, for the rest curves the sensitivities of k_s and D_s both
25 share the same sign and therefore their properties are negatively correlated.

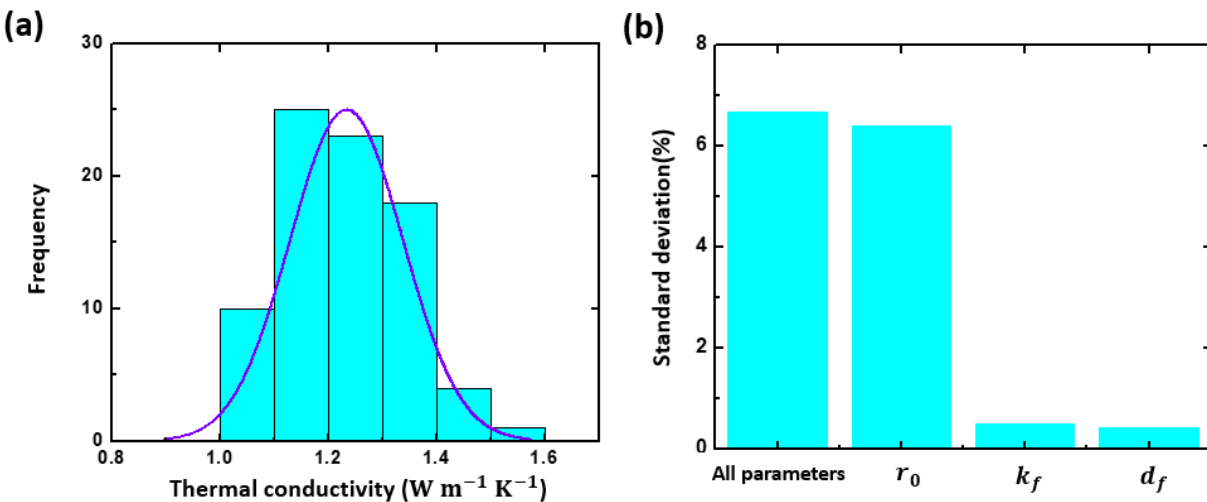
26 5 Error analysis

27 There are multiple factors that influence the reliability of the SPTR technique. The most critical
28 one is the accurate measurement of laser spot size given the extreme sensitivity evidenced by
29 Fig.3 where, in almost all cases, the sensitivity to spot size is larger than that of the thermal
30 properties. Therefore, determining the spot size for each experimental configuration and
31 objective lens choice is of paramount importance. Even for a well-characterized experiment,
32 when the sample surface is not placed at precisely the focal plane of the objective, the change in
33 spot size will impact the fitting results. For example, for a 50× high magnification objective with
34 a short depth of focus, defocusing by 5 μm can change the projected spot size by 9.5% and fitting
35 result by 16%. Therefore, high precision vertical stages with a minimum step size less than 1 μm
36 are recommended for SPTR experimental arrangements.

1 Additional SPTR measurement was conducted on f-SiO₂ under 20× objective and 400 Hz to obtain
 2 a statistical distribution of experimental results for an estimation of experimental repeatability.
 3 The histogram of fitted thermal conductivity is presented in Fig.7(a). The fitted values of thermal
 4 diffusivity follow a normal distribution with a standard deviation of 8.48%.

5 To quantitatively estimate the impact of each parameter on the errors associated with thermal
 6 properties, we apply a Monte Carlo method to the optimization of the multilayer transport model
 7 expressed in Eq.(4) to the experimental data of f-SiO₂ at 20× objective and 400 Hz [50, 51]. Each
 8 of the “controlled parameters” in this implementation of SPTR can influence the total
 9 measurement error, for example the thickness and thermal conductivity of gold film and the
 10 convolved pump-probe spot size. To propagate these errors through our forward model, we first
 11 experimentally measure uncertainties associated with each control parameter. For spot size,
 12 multiple measurements were made to get the value of spot size within a standard deviation of
 13 5%. The errors associated with the thickness and thermal conductivity of film are estimated to
 14 be 2% and 2.4%, respectively. Each parameter is assumed to have a normal distribution around
 15 its mean value with a standard deviation. We fitted the model with updated controlled
 16 parameters to the experimental result repeatedly and obtained the distributions of fitted thermal
 17 properties. The resulting standard deviation is 6.67% that is close to the experimental error
 18 determined through statistics of multiple measurements made on a single sample.

19 Next, the same kind of simulation was repeated when only the finite uncertainty in a single
 20 control parameter – spot size, film thickness, or film thermal conductivity – is considered. The
 21 resulting errors are summarized in Fig.7(b). The standard deviation produced by the uncertainty
 22 of spot size alone is 6.4% and is comparable to the total standard deviation when all controlled
 23 parameters are considered. In contrast, the ultimate uncertainty due to film properties produces
 24 around 1% standard deviation in fitted thermal conductivity; their impact is limited. Based on
 25 Fig.7(b), we conclude that the uncertainty of spot size is clearly the largest source of error.



1 **Fig. 7** (a) Histograms of fitted f-SiO₂ thermal conductivity from SPTR measurement and fitted
2 normal distribution. (b) Standard deviation of fitted normal distribution with all controlled
3 parameters considered as well as standard deviations when the uncertainty of only one
4 controlled parameter is considered.

5 During measurements on f-SiO₂, a spatial variation of reflectance was observed, indicating a
6 partially roughened surface on some areas. The measurements reported in this work were taken
7 on an area with a relatively smooth surface. Such surface roughness was not found on thicker
8 transducer films or on the Ni sample. This could be attributed to the agglomeration of deposited
9 metals on insulating oxides at low temperatures [40, 52]. Rough surfaces can significantly impact
10 the reflectance and produce extra errors in the measurement. Therefore, care should be taken
11 when selecting the film thickness on some substrates and avoiding any surface variations. The
12 small spot sizes used in this type of measurement (1-5 μm) make locally avoiding any small
13 surface imperfections reasonably simple.

14 Errors can also originate from an imperfect square wave excitation and detection. The model
15 expressed in Eqs.(1-4) considers ideal square excitation waves which in practice cannot be
16 achieved due to finite electronic bandwidth. At high frequencies comparable to the laser analog
17 modulation bandwidth and detector bandwidth (500 kHz and 1 MHz, respectively, in this
18 experiment), severe distortion and artifacts of the pump signal have been noticed (e.g.,
19 overshoot, undershoot, and signal delays), likely from Gibbs phenomenon. This influence is
20 severer for SPTR than for FDTR as the square wave is essentially composed of high order
21 harmonic waves. In practice, we find that at a modulation frequency that is 100 times smaller
22 than the detector bandwidth, the pump pulse can be assumed an ideal square without sacrificing
23 accuracy. However, a large bandwidth often comes at a cost of low gain, which subjects the signal
24 to the system's random noise. Therefore, the selection of modulation frequency not only
25 depends on the sensitivity of interested thermal property, but on instrument parameters as well.
26 The electronic characters of the signal processing system must be properly accounted for before
27 high-quality data may be collected.

28 Although these phenomena can be partially alleviated by postprocessing, such as the Lanczos
29 sigma factor, assuming an ideal square wave can lead to an inaccurate estimation of conductivity
30 at high frequency [19]. The imperfect square may result in an underestimation of thermal
31 conductivity by a large margin if not properly accounted for. The components (cables, detector,
32 lasers, etc.) of the system have different responses to different harmonics of the fundamental
33 frequencies expressed in Eq.(1). These responses can be conveniently lumped together as a
34 systematic transfer function [19]. As a result, the forward model requires a modification to
35 analyze the data of imperfect high frequency square pulses by introducing corrections to Eq.(4).
36 The resultant Eq.(5) includes P and ϕ as the amplitude and phase of the systematic transfer
37 function, respectively. To derive these parameters of transfer function, we take a Fourier
38 transform of the imperfect square wave pump signal collected directly by the photodetector at

1 each modulation frequency and compare them with the parameters in Eq.(1). The detailed
2 procedure for applying this correction is described in the appendix.

3 6 Conclusion

4 In summary, we have demonstrated an SPTR technique to measure thermal properties for a wide
5 range of materials and explored the optimal parameter space for measurements. The SPTR
6 technique relies on the thermorefectance principle to monitor the amplitude evolution of
7 surface temperature and has advantages compared to other thermophysical characterization
8 techniques, such as ease of operation, fast data acquisition, and compact instrumentation. An
9 analytical model is developed to simulate the thermal transport and its implementation for the
10 analysis of the experimental data to extract thermal properties of interest is demonstrated. A
11 sensitivity analysis demonstrates that the optimal transducer thickness, spot size, and
12 modulation frequency depend on the thermal properties of the sample. We have validated the
13 SPTR technique and found a good agreement with the literature on several reference samples
14 with thermal conductivity in the range of $1\text{--}100\text{ W}\cdot\text{m}^{-1}\cdot\text{K}^{-1}$. A measurement error of around 10%,
15 mostly originating from the uncertainty of the applied laser spot size, is confirmed through a
16 Monte Carlo analysis. Limitations of the technique, particularly high sensitivity to laser spot size
17 and wave distortion at high frequencies, are discussed. This approach provides an attractive
18 solution for applications where extensive optical alignment is not feasible and offers an
19 opportunity to measure thermal property in a fast and convenient fashion with high accuracy
20 and resolution. The compact and fiberized nature of this and other possible experimental
21 arrangements offers a promising route for the development of multi-analytical tools for
22 expedited materials design and discovery.

23

24 Acknowledgment

25 Y.W., C.A.D., R.S., D.M., and G.B. acknowledge support from the Nuclear Materials Discovery
26 and Qualification initiative (NMDQi) program under the US Department of Energy, Office of
27 Nuclear Energy under Idaho Operations Office (DE-AC07-05ID14517). Y.W., Z.H, and D.H.H.
28 acknowledge support from the Center for Thermal Energy Transport under Irradiation, an
29 Energy Frontier Research Center funded by the US Department of Energy, Office of Science,
30 Office of Basic Energy Science. V.C. and M.K. acknowledge the finical support from the Nuclear
31 Regulatory Commission Faculty Development Program.

32 Conflict of interest

33 The authors declare that they have no conflict of interest.

34 Data and code availability

35 The data and code that support the findings of this study are available from the corresponding
36 authors upon reasonable request.

1 Appendix

2 Ideally, a square wave can be expressed by Eq.(1). Each harmonic has an equal phase of zero and
3 a $1/(2n-1)$ amplitude. In an actual experiment, however, the signal is processed by various
4 electrical circuits which inevitably introduce distortions. These distortions are most often
5 frequency dependent. To conveniently capture these effects, we use a lumped transfer function
6 to account for the changes to both amplitude and phase.

7 First, the imperfect square pulse is measured by removing the short-pass filter normally placed
8 in front of the detector to reject any pump light, shutting down the probe laser, and collecting
9 the pump signal reflected by sample surface using the photodetector.

10 Next, to derive the transfer function, we express the collected non-ideal square wave as

$$x'(t) = \sum_{m=-\infty}^{\infty} P_m \frac{\exp(im\omega t + i\phi_m)}{m} \quad (\text{A1})$$

11 where m are odd integers. Taking advantage of the relation $\int \sin(mt) \sin(nt) dt = \delta_{nm}$ (δ is
12 Kronecker delta function), we can obtain the following relations

$$P_{m,1} = \int_0^{1/f} mx'(t) \cos(m\omega t) dt$$
$$P_{m,2} = \int_0^{1/f} mx'(t) \sin(m\omega t) dt, \quad (\text{A2})$$

13 from which the factors P_m and ϕ_m can be expressed as

$$P_m = \sqrt{P_{m,1}^2 + P_{m,2}^2}$$
$$\phi_m = \text{atan} \left(\frac{P_{m,2}}{P_{m,1}} \right). \quad (\text{A3})$$

14

15 References

- 16 1. D.G. Cahill, P.V. Braun, G. Chen, D.R. Clarke, S. Fan, K.E. Goodson, P. Keblinski, W.P. King, G.D.
17 Mahan, A. Majumdar, H.J. Maris, S.R. Phillpot, E. Pop, L. Shi, Appl. Phys. Rev. 1 (1), 011305 (2014)
18 doi:10.1063/1.4832615
- 19 2. M. Khafizov, V. Chauhan, Y. Wang, F. Riyad, N. Hang, D. Hurley, J. Mater. Res. 32 (1), 204 (2016)
20 doi:<https://doi.org/10.1557/jmr.2016.421>
- 21 3. R. Spotnitz, J. Franklin, J. Power Sources 113 (1), 81 (2003) doi:[https://doi.org/10.1016/S0378-](https://doi.org/10.1016/S0378-7753(02)00488-3)
22 [7753\(02\)00488-3](https://doi.org/10.1016/S0378-7753(02)00488-3)
- 23 4. W. Liu, Q. Jie, H.S. Kim, Z. Ren, Acta Mater. 87, 357 (2015)
24 doi:<https://doi.org/10.1016/j.actamat.2014.12.042>
- 25 5. M. Khandelwal, M.M. Mench, J. Power Sources 161 (2), 1106 (2006)
26 doi:<https://doi.org/10.1016/j.jpowsour.2006.06.092>
- 27 6. S. Huxtable, D.G. Cahill, V. Fauconnier, J.O. White, J.-C. Zhao, Nat. Mater. 3 (5), 298 (2004)
28 doi:10.1038/nmat1114
- 29 7. D. Hurley, M. Khafizov, S. Shinde, J. Appl. Phys. 109 (8), 083504 (2011) doi:10.1063/1.3573511

- 1 8. Z. Hua, J. Spackman, H. Ban, *Materialia* 5, 100230 (2019)
- 2 doi:<https://doi.org/10.1016/j.mtla.2019.100230>
- 3 9. X. Bai, M. Tonks, Y. Zhang, J. Hales, *J. Nucl. Mater.* 470, 208 (2016)
- 4 doi:10.1016/j.jnucmat.2015.12.028
- 5 10. M. Khafizov, J. Pakarinen, L. He, D.H. Hurley, *J. Am. Ceram. Soc* 102 (12), 7533 (2019)
- 6 doi:10.1111/jace.16616
- 7 11. J.A. Aguiar, A.M. Jokisaari, M. Kerr, R. Allen Roach, *Nat. Commun.* 11 (1), 2556 (2020)
- 8 doi:10.1038/s41467-020-16406-2
- 9 12. J.J. de Pablo, N.E. Jackson, M.A. Webb, L.-Q. Chen, J.E. Moore, D. Morgan, R. Jacobs, T. Pollock,
- 10 D.G. Schlom, E.S. Toberer, J. Analytis, I. Dabo, D.M. DeLongchamp, G.A. Fiete, G.M. Grason, G. Hautier, Y.
- 11 Mo, K. Rajan, E.J. Reed, E. Rodriguez, V. Stevanovic, J. Suntivich, K. Thornton, J.-C. Zhao, *npj Comput.*
- 12 *Mater.* 5 (1), 41 (2019) doi:10.1038/s41524-019-0173-4
- 13 13. D. Zhao, X. Qian, X. Gu, S.A. Jajja, R. Yang, *J. Electron. Packag.* 138 (4), (2016)
- 14 doi:10.1115/1.4034605
- 15 14. W. Capinski, H. Maris, *Rev. Sci. Instrum.* 67 (8), 2720 (1996) doi:10.1063/1.1147100
- 16 15. K. Chen, B. Song, N.K. Ravichandran, Q. Zheng, X. Chen, H. Lee, H. Sun, S. Li, G.A.G. Udalamatta
- 17 Gamage, F. Tian, Z. Ding, Q. Song, A. Rai, H. Wu, P. Koirala, A.J. Schmidt, K. Watanabe, B. Lv, Z. Ren, L.
- 18 Shi, D.G. Cahill, T. Taniguchi, D. Broido, G. Chen, *Science* 367 (6477), 555 (2020)
- 19 doi:10.1126/science.aaz6149
- 20 16. C. Wei, X. Zheng, D. Cahill, J. Zhao, *Rev. Sci. Instrum.* 84 (7), 071301 (2013)
- 21 doi:10.1063/1.4815867
- 22 17. J. Ravichandran, A.K. Yadav, R. Cheaito, P.B. Rossen, A. Soukiassian, S.J. Suresha, J.C. Duda, B.M.
- 23 Foley, C.-H. Lee, Y. Zhu, A.W. Lichtenberger, J.E. Moore, D.A. Muller, D.G. Schlom, P.E. Hopkins, A.
- 24 Majumdar, R. Ramesh, M.A. Zurbuchen, *Nat. Mater.* 13 (2), 168 (2014) doi:10.1038/nmat3826
- 25 18. F. Hofmann, M.P. Short, C.A. Dennett, *MRS Bull.* 44 (5), 392 (2019) doi:DOI:
- 26 10.1557/mrs.2019.104
- 27 19. S. Middlemas, Z. Hua, V. Chauhan, W.T. Yorgason, R. Schley, A. Khanolkar, M. Khafizov, D.
- 28 Hurley, *J. Nucl. Mater.* 528, 151842 (2020) doi:<https://doi.org/10.1016/j.jnucmat.2019.151842>
- 29 20. D.H. Olson, J.L. Braun, P.E. Hopkins, *J. Appl. Phys.* 126 (15), 150901 (2019)
- 30 doi:10.1063/1.5120310
- 31 21. A.J. Schmidt, X. Chen, G. Chen, *Rev. Sci. Instrum.* 79 (11), 114902 (2008) doi:10.1063/1.3006335
- 32 22. D. Cahill, *Rev. Sci. Instrum.* 75 (12), 5119 (2004) doi:10.1063/1.1819431
- 33 23. J. Feser, J. Liu, D. Cahill, *Rev. Sci. Instrum.* 85 (10), 104903 (2014) doi:10.1063/1.4897622
- 34 24. C. Chiritescu, D. Cahill, N. Nguyen, D. Johnson, A. Bodapati, P. Keblinski, P. Zschack, *Science* 315
- 35 (5810), 351 (2007) doi:10.1126/science.1136494
- 36 25. M. Li, J.S. Kang, Y. Hu, *Rev. Sci. Instrum.* 89 (8), 084901 (2018) doi:10.1063/1.5026028
- 37 26. A.J. Schmidt, R. Cheaito, M. Chiesa, *Rev. Sci. Instrum.* 80 (9), 094901 (2009)
- 38 doi:10.1063/1.3212673
- 39 27. L. Tang, C. Dames, *Int. J. Heat Mass Transf.* 164, 120600 (2021)
- 40 doi:<https://doi.org/10.1016/j.ijheatmasstransfer.2020.120600>
- 41 28. J. Malen, K. Baheti, T. Tong, Y. Zhao, J. Hudgings, A. Majumdar, *J. Heat Trans.-T. ASME* 133 (8),
- 42 (2011) doi:10.1115/1.4003545
- 43 29. D. Hurley, R. Schley, M. Khafizov, B. Wendt, *Rev. Sci. Instrum.* 86 (12), 123901 (2015)
- 44 doi:10.1063/1.4936213
- 45 30. Y. Wang, D.H. Hurley, E.P. Luther, M.F. Beaux, D.R. Vodnik, R.J. Peterson, B.L. Bennett, I.O. Usov,
- 46 P. Yuan, X. Wang, M. Khafizov, *Carbon* 129, 476 (2018)
- 47 doi:<https://doi.org/10.1016/j.carbon.2017.12.041>
- 48 31. J. Hartmann, P. Voigt, M. Reichling, *J. Appl. Phys.* 81 (7), 2966 (1997) doi:10.1063/1.364329

1 32. D. Fournier, M. Marangolo, C. Fretigny, J. Appl. Phys. 128 (24), 241101 (2020)
2 doi:10.1063/5.0019025

3 33. J.L. Braun, D.H. Olson, J.T. Gaskins, P.E. Hopkins, Rev. Sci. Instrum. 90 (2), 024905 (2019)
4 doi:10.1063/1.5056182

5 34. D. Hurley, O. Wright, O. Matsuda, S. Shinde, J. Appl. Phys. 107 (2), 023521 (2010)
6 doi:10.1063/1.3272827

7 35. C. Cardell, I. Guerra, Trends Anal. Chem 77, 156 (2016)
8 doi:<https://doi.org/10.1016/j.trac.2015.12.001>

9 36. K. Hatori, N. Taketoshi, T. Baba, H. Ohta, Rev. Sci. Instrum. 76 (11), 114901 (2005)
10 doi:10.1063/1.2130333

11 37. A. Yurai, T. Nakanishi, Rev. Sci. Instrum. 78 (5), 054903 (2007) doi:10.1063/1.2736414

12 38. P.E. Raad, In Electronics Cooling Magazine, (2008),

13 39. J. Liu, J. Zhu, M. Tian, X. Gu, A. Schmidt, R. Yang, Rev. Sci. Instrum. 84 (3), 034902 (2013)
14 doi:10.1063/1.4797479

15 40. A.J. Schmidt, R. Cheaito, M. Chiesa, J. Appl. Phys. 107 (2), 024908 (2010) doi:10.1063/1.3289907

16 41. G. Langer, J. Hartmann, M. Reichling, Rev. Sci. Instrum. 68 (3), 1510 (1997)
17 doi:10.1063/1.1147638

18 42. Handbook of Chemistry and Physics. 99 edition edn. (CRC Press, 2018),

19 43. P.E. Hopkins, P.M. Norris, R.J. Stevens, J. Heat Trans -T ASME 130 (2), (2008)
20 doi:10.1115/1.2787025

21 44. M. Ahadi, M. Andisheh-Tadbir, M. Tam, M. Bahrami, International Journal of Heat and Mass
22 Transfer 96, 371 (2016) doi:<https://doi.org/10.1016/j.ijheatmasstransfer.2016.01.037>

23 45. Z. Hua, H. Ban, D.H. Hurley, Rev. Sci. Instrum. 86 (5), 054901 (2015) doi:10.1063/1.4919609

24 46. X. Zheng, D.G. Cahill, P. Krasnochtchekov, R.S. Averback, J.C. Zhao, Acta Mater. 55 (15), 5177
25 (2007) doi:<https://doi.org/10.1016/j.actamat.2007.05.037>

26 47. D.R. Queen, F. Hellman, Rev. Sci. Instrum. 80 (6), 063901 (2009) doi:10.1063/1.3142463

27 48. B.C. Gundrum, D.G. Cahill, R.S. Averback, Phys. Rev. B 72 (24), 245426 (2005)
28 doi:10.1103/PhysRevB.72.245426

29 49. Y.-J. Wu, L. Fang, Y. Xu, npj Comput. Mater. 5 (1), 56 (2019) doi:10.1038/s41524-019-0193-0

30 50. J. Yang, E. Ziade, A.J. Schmidt, Rev. Sci. Instrum. 87 (1), 014901 (2016) doi:10.1063/1.4939671

31 51. W. Shen, D. Vaca, S. Kumar, Nanosc. Microsc. Therm. 24 (3-4), 138 (2020)
32 doi:10.1080/15567265.2020.1807662

33 52. P.R. Gadkari, A.P. Warren, R.M. Todi, R.V. Petrova, K.R. Coffey, J. Vac. Sci. Technol. A 23 (4),
34 1152 (2005) doi:10.1116/1.1861943

35